JOURNAL OF PROPULSION AND POWER
Vol. 11, No. 4, July–August 1995

Hot Fragment Conductive Ignition of Nitramine-Based Propellants

T. H. Huang,* S. T. Thynell,† and K. K. Kuo‡
Pennsylvania State University, University Park, Pennsylvania 16802

Hot fragments generated during the impact of shaped-charge jets may penetrate the cartridge casing and induce propellant ignition. The major objective of this study is to acquire a better understanding of hot fragment conductive ignition behavior of nitramine-based XM39 and M43 propellants. The confinement effect of the cartridge is simulated by an enclosure within which the pyrolysis products can accumulate and significantly increase pressure. Both theory and experiments showed that the ignition threshold was a strong function of confinement. At low pressures, the XM39 propellant was more susceptible to ignition, because its binder decomposition is more exothermic than that of the M43 propellant. At highly confined conditions, which allow for chamber pressurization, the M43 ignition threshold became lower than that of XM39 propellant. The reduction of the ignition threshold is caused mainly by exothermic reactions between CH_2O and NO_2 species, which are enhanced under gas accumulation conditions.

Nomenclature

A = Arrhenius frequency factor
A_{exit} = area of chamber exhaust port, m^2
A_i = interface area between liquid melt and gas bubbles, m^2
A_s = interface area between foam layer and propellant, m^2
A_{side} = interface area between foam layer and gas-phase region, m^2
A_{sp} = surface area of spall particle exposed to gas phase, m^2
C_p = constant-pressure specific heat, J/kg-K
C_v = constant-volume specific heat, J/kg-K
E = activation energy, J/mole
h = specific enthalpy, J/kg
k_i = rate constant specified in Table 2
L_m = height of melt or foam layer, m
L_s = height of spall particle, m
m = mass, kg
$\dot{m}_{g\,net}$ = net rate of production of gaseous mass in foam layer, kg/s
$\dot{m}_{in}$ = mass flow rate into gas phase from foam layer, kg/s
$\dot{m}_{out}$ = mass flow rate of gas out of confinement region, kg/s
P_g = chamber pressure, Pa
$\dot{q}''_{gas}$ = heat flux from spall particle base to gas phase, W/m^2
Q_L = heat release due to desorption from liquid melt to gas bubbles, J/kg
Q_{melt} = heat of endothermic reaction from solid propellant to liquid melt, J/kg
$\dot{q}''_{gas\text{-}li}$ = heat flux from gas phase to liquid phase through interfaces, W/m^2
$\dot{q}''_{gas\text{-}wall}$ = heat flux from chamber gas to chamber wall, W/m^2
$\dot{q}''_{li}$ = heat flux from spall particle base to liquid phase, W/m^2
$\dot{q}''_{liq\text{-}solid}$ = heat flux from foam layer to propellant surface, W/m^2
$\dot{q}''_{sp\text{-}gas}$ = heat flux from spall particle to gas-phase region, W/m^2
R_u = universal gas constant, 8314.4 J/kg-mole K
r = radial coordinate, m
r_{pr} = radius of propellant, m
r_s = radius of spall particle, m
T_g = bulk temperature of gas in chamber, K
T_{gf} = mean gas-bubble temperature in foam layer, K
T_{lf} = mean liquid temperature in foam layer, K
T_{melt} = melting temperature of propellant, K
T_{SB} = temperature of bottom surface of spall, K
t = time, s
u = specific internal energy, J/kg
V_{lr} = velocity of liquid in foam layer into gas-phase region, m/s
V_{lrg} = velocity of gas in foam layer into gas-phase region, m/s
V_s, $-V_m$ = sinking velocity of spall particle, m/s
Y = mass fraction
z = axial distance above base of spall particle, m
ΔH_f^0 = heat of formation, J/kg
ΔH_r = heat of reaction, J/g
γ = specific heat ratio
λ = thermal conductivity, W/m-K
ξ_{ji} = mass fraction of ith dissolved gaseous species in jth component of liquid
ρ = density, kg/m^3
Ψ = average porosity (void fraction) of foam layer
$\dot{\omega}_i$ = rate of formation of ith species in gas phase, kg/s

Subscripts
con, 1 = conversion of $RDX_{(l)}$ to $CH_2O_{(dgl)}$ and $N_2O_{(dgl)}$ at rate of k_1
con, 2 = conversion of $RDX_{(l)}$ to $HCN_{(dgl)}$ and $HONO_{(dgl)}$ at rate of k_2
dgl = dissolved gas in liquid
g = gas phase in chamber
gf = gas bubble in foam layer
i = initial condition
lf = liquid phase in foam layer

Received Aug. 6, 1994; revision received January 17, 1995; accepted for publication Jan. 30, 1995.

*Graduate Research Assistant of Fuel Science.
†Associate Professor of Mechanical Engineering. Member AIAA.
‡Distinguished Professor of Mechanical Engineering. Fellow AIAA.

melt = melt layer
pr = propellant
s = spall fragment

I. Introduction

THE purpose of performing hot fragment conductive ignition (HFCI) studies is to further the development of technology for better assessment of the survivability of weapon systems (such as tanks, ships, etc.), containing stowed ammunition. Hot fragments are inevitably generated from the penetration of armor plates by shaped-charge jets or kinetic-energy penetrators. One way to negate the threat of propellant ignition by hot fragments is to use a propellant that is resistant to conductive ignition. In recent years, considerable effort has been devoted to the development of low vulnerability ammunition (LOVA) and high energy LOVA (HELOVA) propellants.

Raley et al.[1] conducted experiments using a chemical energy (CE) spall test in order to evaluate the response of candidate propellants for 105-mm tank cannon ammunition to a shaped-charge jet-generated spall attack. In these experiments, nitrocellulose-based (M30) and nitramine-based (XM39 LOVA and M43 HELOVA) propellants were employed. Previously conducted HFCI tests indicated that the M43 propellant should be less susceptible to ignition due to spall fragment-induced pyrolysis and reaction than the XM39 propellant. It was expected that similar results would be obtained with CE-spall tests using these propellants confined within ammunition cartridges. However, test firings revealed that none of the cartridges loaded with the XM39 LOVA propellant reacted when attacked by spall fragments, whereas about 25% of the cartridges loaded with the HELOVA propellant (M43) exploded after first producing smoke during fizz burning (slow cookoff) for about 65–125 s. The XM39 and M43 propellants contain the same nitramine (RDX), and the only difference is that an acetyl triethyl citrate (ATEC) binder ingredient in XM39 propellant is replaced with an energetic plasticizer (EP) in M43 propellant.

It was postulated that the difference in the conditions under which the HFCI and CE spall tests were conducted may be the cause of the unexpected results. Specifically, the HFCI tests were conducted at constant pressures, whereas the penetration of spall fragments through the cartridge casing may lead to a pressure rise caused by an accumulation of pyrolysis products within the cartridge and subsequent gas-phase ignition among pyrolysis products. The possibility of pressure increase could be caused by a rearrangement of the granular bed, i.e., the entrance hole of the shaped-charge jet for spall fragment generation is partially blocked, thus preventing pyrolysis gases to escape.

The overall objective of this study is to understand and assess the thermochemical processes controlling the ignition susceptibility of XM39 (LOVA) and M43 (HELOVA) propellants and to explain the unexpected ignition behavior of

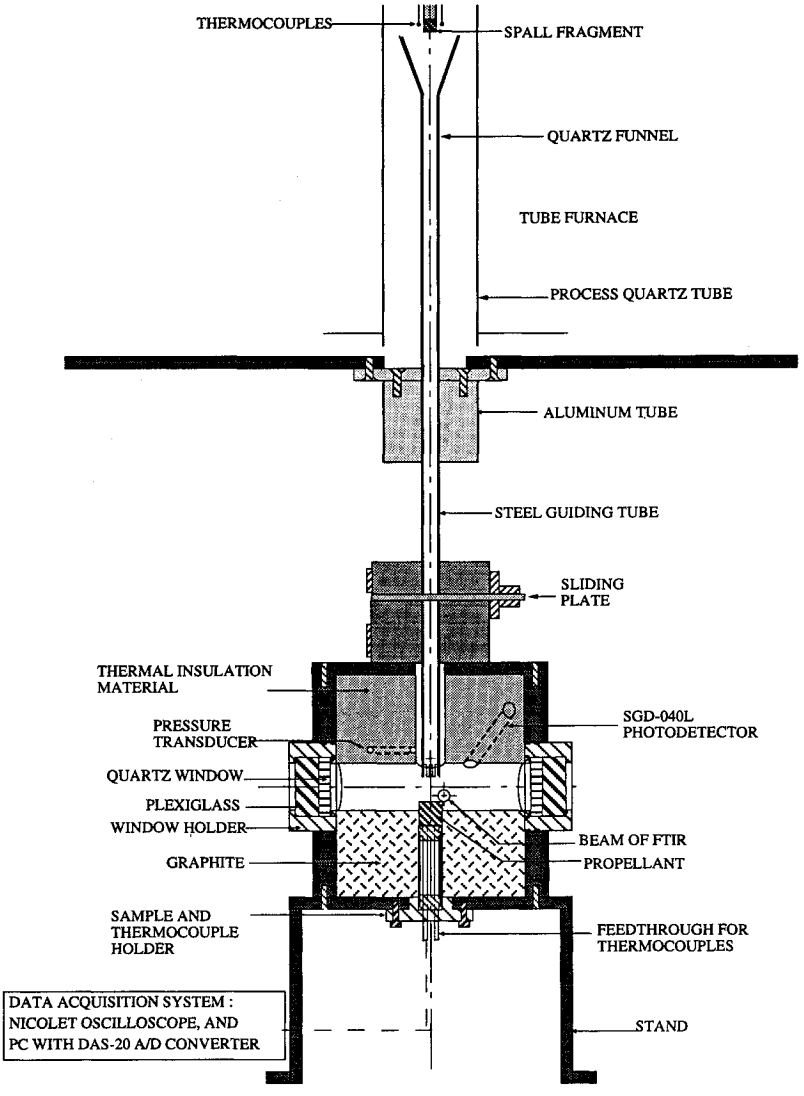

Fig. 1 Schematic diagram of test rig for conducting confined hot fragment conductive ignition studies.

M43 propellants within confined enclosures. Such a study involved the design of a partially confined (PCHFCI) test setup for simulating the effect of gas accumulation on ignition within a cartridge damaged by spall fragments and the extension of an existing theoretical model to include the effect of the confined enclosure and binder ingredient differences.

II. Experimental Approach

In this study, a stainless steel cylinder of diameter 0.63 cm (0.25 in.) was used to simulate the spall fragment. The selection of this geometry had two advantages: 1) the bottom surface is flat, which should enable a good contact with the propellant surface; and 2) the experimental results can be compared with results obtained from the PCHFCI model.

The fragment was suspended in the hot-core region of the tube furnace, shown at the top of Fig. 1, by the suction force produced from the vacuum in a stainless steel tube. After the fragment reached thermal equilibrium within the furnace, the fragment was released, falling downward through an open section at the bottom of the furnace by gas filling of the vacuum. A quartz funnel and a stainless steel tube (8 mm i.d.) were used to guide the fragment into the confined enclosure. When the cylindrical fragment landed on the sample, nitrogen gas from a cylinder pushed a sliding plate to close the opening of the guiding tube to prevent pyrolyzed gases from entering and igniting within the furnace. Closing the opening at the top of the chamber also allowed pressure buildup in highly confined test situations. An O-ring provided a pressure seal under the sliding plate. The nitrogen gas line was controlled by a remote control ball valve. A perforated exhaust hood, located directly below the furnace, was employed to remove the pyrolysis gases in case of leakage.

The test rig allows for temperature, pressure, and light emission measurements. The test chamber is made of stainless steel of circular cylinder shape. The o.d. of the chamber is 12.7 cm (5 in.), and the length is 12.7 cm. Graphite and thermal insulation material were installed inside the chamber. The internal volume of the chamber is approximately 57 cm^3. Two sealed viewing windows were set up with double layers of quartz on the inside and Plexiglas® on the outside. The landing of the spall fragment on the propellant sample was recorded by a video camera through the viewing windows. The test chamber can be highly confined when the relief ball valve is tightly closed and a high-pressure bursting diaphragm is installed in the safety head. During the highly confined tests, the maximum chamber pressure is controlled by choosing the appropriate bursting diaphragm.

A wide variety of measurements was performed in the test rig while the hot fragment interacted with the propellant. These included 1) transient temperature response within solid propellant at several locations, 2) onset of light emission and subsequent ignition of sample by a fast-response near-IR photodetector, 3) time variations of gas-phase temperatures at several locations within the enclosure, 4) pressure-time variation within the enclosure, and 5) observation of gaseous ignition and combustion processes by means of a video camera.

III. Theoretical Study

In the theoretical portion of the investigation, an existing HFCI model[2-5] was extended by incorporating a reduced chemical kinetic mechanism of M43 propellant and by accounting for the gas accumulation effect in the confined environment. To provide strong linkage between the modeling effort and experiment, the model was formulated to simulate the experimental test event including 1) a uniformly heated metal particle; 2) a realistic propellant sample; 3) heat conduction induced ignition phenomena; 4) chamber pressurization, due to accumulation of gas-phase products; and 5) effect of chamber confinement on go/no-go ignition boundary.

The chemical composition of XM39 propellant is listed in Table 1. The RDX crystals are on average 5 μm in diameter, and are bound together primarily by the CAB and ATEC ingredients. The competing decomposition reactions of RDX are considered together with the major exothermic reaction between NO_2 and CH_2O. A detailed description of the chemical kinetic scheme for ignition study of XM39 propellant is given in Table 2. The mechanism proposed by Brill and Brush[6] and associated kinetic data suggested by Melius[7] were adopted for RDX decomposition. The DSC data of XM39 obtained by Miller[8] were used for the liquid-to-gas conversion rate. The global kinetic rates for reactions between NO_2 and CH_2O were adopted from the work of BenReuven et al.[9] Because of its chemical stability, the effects of EC on ignition were assumed to be negligible.

The simplified chemical kinetics of M43 propellant are also shown in Table 2. The only difference from those of XM39 is the replacement of ATEC decomposition by EP decomposition. The decomposition of EP is more endothermic than that of ATEC.

In formulating the theoretical model, four sets of governing equations, as well as their boundary and initial conditions, were derived. These governing equations were formulated by considering that the hot spall particle be adequately treated by transient two-dimensional axisymmetric heat conduction, the LOVA propellant be treated as a transient heat-conduction region with surface regression, the foam layer solved as a reacting two-phase region, and the gas-phase region be treated by a lumped parameter analysis. Reference 2 contains a thorough discussion of most of the HFCI model assumptions. The lumped parameter analysis is based on the expectation that the gases evolved from the foam layer into the gas-phase region have sufficient momentum to mix and slowly react. This should be a reasonable assumption since ignition delay times are approximately 60 to 120 s. The governing equations for each region are given below.

A. Energy Equation of Hot Spall Fragment

To determine the temperature profile in the cylindrical spall fragment, as well as the average temperature at its base, the following transient two-dimensional heat conduction equation is considered:

$$\frac{\partial}{\partial t}(\rho_s C_s T_s) = \frac{1}{r}\frac{\partial}{\partial r}\left(\lambda_s r \frac{\partial T_s}{\partial r}\right) + \frac{\partial}{\partial z}\left(\lambda_s \frac{\partial T_s}{\partial z}\right) \tag{1}$$

B. Energy Equation of Propellant

Since the heat transfer is primarily one dimensional from the spall fragment to the solid propellant, radial temperature variations in the propellant are negligible. A transient one-dimensional heat conduction equation is given as

$$\frac{\partial}{\partial t}(\rho_{\mathrm{pr}} C_{p,\mathrm{pr}} T_{\mathrm{pr}}) = \frac{\partial}{\partial z}\left(\lambda_{\mathrm{pr}} \frac{\partial T_{\mathrm{pr}}}{\partial z}\right) \tag{2}$$

for solving the thermal profile in the propellant beneath the spall particle.

C. Analysis of Foam Layer

The physical and chemical processes occurring in liquid and gas bubbles within the foam layer are treated separately, as shown in Fig. 2.

Mass continuity of gas bubbles

$$\frac{\mathrm{D}}{\mathrm{D}t}(m_{\mathrm{gf}}) = -\dot{m}_{\mathrm{gf},r} + \dot{m}_{g\mathrm{net}} \tag{3}$$

where $m_{\mathrm{gf}} = \rho_{\mathrm{gf}} \Psi L_m \pi r_{\mathrm{pr}}^2$, $\dot{m}_{\mathrm{gf},r} = \rho_{\mathrm{gf}} V_{\mathrm{lrg}} \Psi A_{\mathrm{side}}$, and $\dot{m}_{g\mathrm{net}} = \rho_{\mathrm{lf}} k_3 (1 - \Psi) L_m \pi r_{\mathrm{pr}}^2$.

Table 1 Chemical composition of XM39 propellant

Ingredient name	Chemical composition	Molecular weight, kg/kmole	Mass fraction, %	ΔH_f^0, kJ/kg	ρ, g/cm^3
RDX, 5 μm	$C_3H_6N_6O_6$	222.13	76	276.86	1.82
CAB[a]	$C_{15}H_{22}O_8$	330.0	12	−4933.76	1.22
NC[b]	$C_6H_{7.55}O_5(NO_2)_{2.45}$	272.3	4	−2583.8	1.655
ATEC	$C_{14}H_{22}O_8$	318.3	7.6	5459.6	1.135
EC	$C_{17}H_{20}ON_2$	268	0.4	−391.5	1.14

[a]Cellulose acetate butyrate. [b]Nitrocellulose.

Table 2 Simplified chemical kinetic scheme and rate constants for ignition study of XM39 and M43 propellants

1. XM39 Solid propellant/foam layer interface

$$\text{Solid propellant} \begin{cases} \text{RDX}_{(s)} \\ \text{binder}_{(s)} \end{cases} \rightarrow \text{RDX}_{(l)} + \text{binder}_{(l)} \quad (\Delta H_r = -265.2 \text{ J/g-binder})$$

2. Foam layer

Liquid

$$\text{RDX}_{(l)} \xrightarrow{k_1} 3\,\text{CH}_2\text{O}_{(dgl)} + 3\,\text{N}_2\text{O}_{(dgl)} \quad (\Delta H_r = -894.4 \text{ J/g-RDX})$$

$$\text{RDX}_{(l)} \xrightarrow{k_2} 3\,\text{HCN}_{(dgl)} + 3\,\text{HONO}_{(dgl)}$$

$$\xrightarrow{\text{Fast}} 3\,\text{HCN}_{(dgl)} + \tfrac{3}{2}\,\text{NO}_{(dgl)} + \tfrac{3}{2}\,\text{NO}_{2(dgl)} + \tfrac{3}{2}\,\text{H}_2\text{O}_{(dgl)} \quad (\Delta H_r = 587.1 \text{ J/g-RDX})$$

$$\text{Binder}_{(l)} \xrightarrow{\text{Fast}} \begin{cases} \text{ATEC} \longrightarrow 5\,\text{CH}_2\text{O}_{(dgl)} + 3\,\text{C}_2\text{H}_{4(dgl)} + 3\,\text{CO}_{(dgl)} & \text{(for XM39)} \\ \text{EP} \longrightarrow 4\,\text{NO}_2 + 2\,\text{CH}_2\text{O} + \text{C}_2\text{H}_2 + \text{CH}_4 + \text{C}_2\text{H}_4 & \text{(for M43)} \\ \text{NC} \longrightarrow 2.45\,\text{NO}_{2(dgl)} + 2\,\text{CH}_2\text{O}_{(dgl)} + 2\,\text{CO}_{(dgl)} + \text{C}_2\text{H}_{2(dgl)} + \text{H}_2\text{O}_{(dgl)} & \text{(for either XM39 or M43)} \\ \text{CAB} \longrightarrow 6\,\text{CH}_2\text{O}_{(dgl)} + 3\,\text{C}_2\text{H}_{2(dgl)} + \text{CH}_{4(dgl)} + 2\,\text{CO}_{(dgl)} & \end{cases}$$

Liquid/gas bubble interface

$$A_{i(l)} \xrightarrow{k_3} A_{i(g)} \quad (\Delta H_v = 322.6 \text{ J/g-liq})$$

Where A_i includes RDX, CH_2O, N_2O, HCN, NO, NO_2, H_2O, C_2H_4, CO, C_2H_2, and CH_4

Gas bubbles

$$\text{RDX}_{(g)} \xrightarrow{k_1} 3\,\text{CH}_2\text{O}_{(g)} + 3\,\text{N}_2\text{O(g)} \quad (\Delta H_r = -1318.4 \text{ J/g-RDX})$$

$$\text{RDX}_{(g)} \xrightarrow{k_2} 3\,\text{HCN}_{(g)} + \tfrac{3}{2}\,\text{NO}_{(g)} + \tfrac{3}{2}\,\text{NO}_{2(g)} + \tfrac{3}{2}\,\text{H}_2\text{O}_{(g)} \quad (\Delta H_r = 162.6 \text{ J/g-RDX})$$

$$\text{NO}_{2(g)} + \tfrac{5}{7}\,\text{CH}_2\text{O}_{(g)} \xrightarrow{k_4} \text{NO}_{(g)} + \tfrac{2}{7}\,\text{CO}_{2(g)} + \tfrac{3}{7}\,\text{CO}_{(g)} + \tfrac{5}{7}\,\text{H}_2\text{O}_{(g)} \quad (\Delta H_r = -4182.5 \text{ J/g-NO}_2)$$

3. Gas-phase region

$$\text{RDX}_{(g)} \xrightarrow{k_1} 3\,\text{CH}_2\text{O}_{(g)} + 3\,\text{N}_2\text{O}_{(g)}$$

$$\text{RDX}_{(g)} \xrightarrow{k_2} 3\,\text{HCN}_{(g)} + \tfrac{3}{2}\,\text{NO}_{(g)} + \tfrac{3}{2}\,\text{NO}_{2(g)} + \tfrac{3}{2}\,\text{H}_2\text{O}_{(g)}$$

$$\text{NO}_{2(g)} + \tfrac{5}{7}\,\text{CH}_2\text{O}_{(g)} \xrightarrow{k_4} \text{NO}_{(g)} + \tfrac{2}{7}\,\text{CO}_{2(g)} + \tfrac{3}{7}\,\text{CO}_{(g)} + \tfrac{5}{7}\,\text{H}_2\text{O}_{(g)}$$

$k_i = A \exp[-E/RuT]$	A	E, Kcal/g mole	Reference
k_1	1×10^{13}, (1/s)	36.0	6 and 7
k_2	2×10^{16}, (1/s)	45.0	6 and 7
k_3	1.98×10^{14}, (1/s)	38.2	8
k_4	10^{12}, (cm^3/g mole-s)	19.0	9

Mass continuity of liquid melt

$$\frac{\mathrm{D}}{\mathrm{D}t}(m_{\text{lf}}) = \dot{m}_{\text{pr}} - \dot{m}_{\text{lf},r} - \dot{m}_{g\text{net}} \tag{4}$$

where $m_{\text{lf}} = \rho_{\text{lf}}(1 - \Psi)L_m\pi r_{\text{pr}}^2$, $\dot{m}_{\text{lf},r} = \rho_{\text{lf}}V_{\text{lr}}(1 - \Psi)A_{\text{side}}$, and $\dot{m}_{\text{pr}} = \rho_{\text{pr}}(-V_m)A_s$.

Energy conservation of gas bubbles

$$\frac{\mathrm{D}}{\mathrm{D}t}(m_{\text{gf}}u_{\text{gf}}) = -\dot{m}_{\text{gf},r}h_{\text{gf}} + \dot{m}_{g\text{net}}Q_L + \Psi\dot{q}''_{\text{gas}}\pi r_{\text{pr}}^2 - \dot{q}''_{\text{gas-liq}}A_i \tag{5}$$

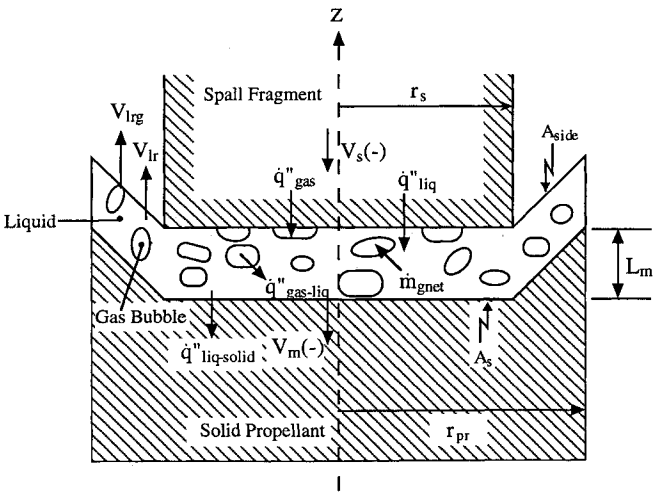

Fig. 2 Schematic diagram showing certain heat and mass fluxes associated with foam layer.

Energy conservation of liquid melt

$$\frac{D}{Dt}(m_{lf}u_{lf}) = -\dot{m}_{lf,r}h_{lf} - \dot{m}_{gnet}Q_L + (1-\Psi)\dot{q}''_{liq}\pi r_s^2 + \dot{q}''_{gas-liq}A_i + \dot{m}_{pr}Q_{melt} - \dot{q}''_{liq-solid}A_s \quad (6)$$

Species conservation of liquid phase

$$\frac{D}{Dt}(Y_{lf,1}m_{lf}) = (-\dot{m}_{lf,r} - \dot{m}_{gnet})Y_{lf,1} - \dot{m}_{con,1} - \dot{m}_{con,2} + Y_{pr,1}\dot{m}_{pr} \quad (7)$$

$$\frac{D}{Dt}(Y_{lf,2}m_{lf}) = (-\dot{m}_{lf,r} - \dot{m}_{gnet})Y_{lf,2} + \dot{m}_{con,1} \quad (8)$$

$$\frac{D}{Dt}(Y_{lf,3}m_{lf}) = (-\dot{m}_{lf,r} - \dot{m}_{gnet})Y_{lf,3} + \dot{m}_{con,2} \quad (9)$$

where $Y_{lf,1}$ is the mass fraction of RDX in the liquid, $Y_{lf,2}$ is the mass fraction of CH_2O and N_2O (low-temperature pathway), $Y_{lf,3}$ is the mass fraction of HCN, NO, NO_2, and H_2O (high-temperature pathway), $Y_{lf,4}$ is the mass fraction of binder decomposition products in liquid, and $Y_{pr,1}$ is the mass fraction of RDX in the propellant.

Conservation of ith gas-phase species in bubbles (including RDX, CH_2O, N_2O, HCN, NO, NO_2, H_2O, C_2H_4, CO, C_2H_2, CH_4, and CO_2)

$$\frac{D}{Dt}(Y_{gf,i}m_{gf}) = -\dot{m}_{gf,r}Y_{gf,i} + \dot{\omega}_{gf,i} + \dot{m}_{gnet}\sum_{j=1}^{4} Y_{lf,j}\xi_{j,i} \quad (10)$$

where $\dot{\omega}_{gf,i}$ is the rate of production of ith species in the gas bubbles based upon the kinetic rates of k_1, k_2, and k_4.

D. Analysis of Gas-Phase Region Inside Test Chamber

The major assumptions in deriving the governing equations for the gas-phase region include 1) uniform temperatures, pressure, and species concentrations; 2) approximately constant total gas volume; 3) gaseous mixture containing only RDX, CH_2O, N_2O, HCN, NO, NO_2, H_2O, C_2H_4, CO, C_2H_2, CH_4, CO_2 species, and any diluent gas such as N_2; and 4) applicability of ideal gas law.

Mass conservation

$$\frac{D}{Dt}(m_g) = \dot{m}_{lf,r} + \dot{m}_{gf,r} - \dot{m}_{out} \quad (11)$$

where

$$\dot{m}_{out} = A_{exit}\rho_g\sqrt{2C_{p,g}T_g[(P_{amb}/P_g)^{2/\gamma} - (P_{amb}/P_g)^{(\gamma+1)/\gamma}]}$$

for the unchoked flow condition, and

$$\dot{m}_{out} = [2/(\gamma+1)]^{\gamma+1/2(\gamma-1)}A_{exit}P\sqrt{\gamma/RT_g}$$

for the choked flow condition.[10]

Energy conservation

$$\frac{D}{Dt}(m_g u_g) = \dot{m}_{in}h_{in} - \dot{m}_{out}h_{out} + \dot{q}''_{sp-gas}A_{sp} - \dot{q}''_{gas-wall}A_{wall} \quad (12)$$

where u_g, the specific internal energy, is defined as

$$u_g = \sum_{i=1}^{13} u_{g,i}Y_{g,i} \quad \text{and} \quad u_{g,i} = \Delta H^0_{f,i} + \int_{T_0}^{T} C_{v,i}\,dT$$

Species conservation

$$\frac{D}{Dt}(Y_{g,i}m_g) = \dot{m}_{gf,r}Y_{gf,i} - Y_{g,i}\dot{m}_{out} + \dot{m}_{lf,r}\sum_{j=1}^{4} Y_{lf,j}\xi_{j,i} + \dot{\omega}_{g,i} \quad (13)$$

Equation of state

$$P_g = \rho_g R_u T_g \sum_{i=1}^{13}\frac{Y_i}{M_{w,i}} \quad (14)$$

where P_g is gas pressure, T_g is gas temperature, and $M_{w,i}$ is molecular weight of ith species.

IV. Experimental Results and Discussion

The results described in the next sections were obtained by using a spall fragment of 0.63 cm diameter and a propellant sample of 1.1 cm diameter. Variation of mass was achieved by using different heights of spall and propellant samples. The gas present initially within the test chamber was regular air. The size of the exhaust port in the test chamber for the partially confined enclosure was approximately 0.3 cm^2 when the relief ball valve was open. The test chamber can be operated at either the highly or partially confined conditions discussed below. In these experiments, K-type thermocouples with an approximate bead size of 500 and 75 μm were used to record temperatures in the gas-phase region and foam layer, respectively.

A. Partially vs Highly Confined Enclosure

Figure 3 shows a set of temperature-time traces and near-IR photodetector response for the M43 propellant, which first pyrolyzed less than 1 s after contact with the hot cylinder and later ignited around 9 s. The initial temperature of the spall fragment was 1473 K. The near-IR photodetector response reveals a sharp spike shortly after the initial contact. The reduction in recorded response that follows is due to the generation of highly opaque pyrolysis products. From t = 9 s, the near-IR photodetector response shows a plateau level with slight oscillations over a 10-s time interval due to the appearance of flamelets near the sample surface revealed from video images. Thermocouples A and B, initially located at 0.19 cm and 0.67 cm below the sample surface along the edge of the propellant, show a rapid increase in temperature at t = 18 s, and the gas temperatures approach approximately 773 K. Thermocouple C, located at the bottom of the propellant, showed a rapid temperature rise to 1103 K when

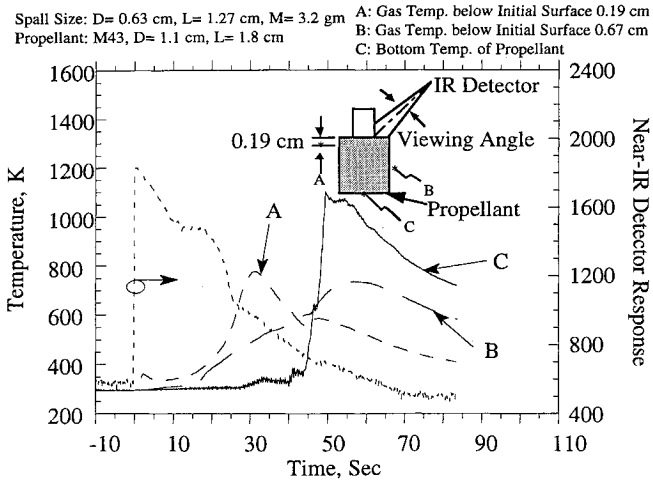

Fig. 3 Recorded temperature-time traces and near-IR photodetector response for M43 propellant in an HFCI test (initial spall temperature = 1473 K).

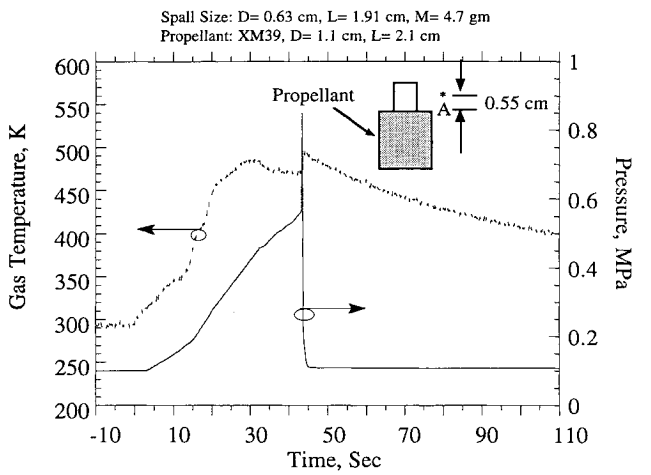

Fig. 4 Recorded temperature and pressure-time traces for XM39 propellant in an HFCI test (initial spall temperature = 1123 K).

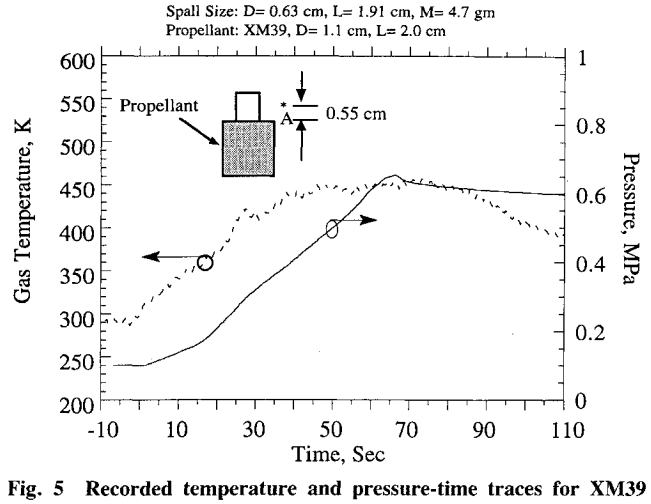

Fig. 5 Recorded temperature and pressure-time traces for XM39 propellant in an HFCI test (initial spall temperature = 1023 K).

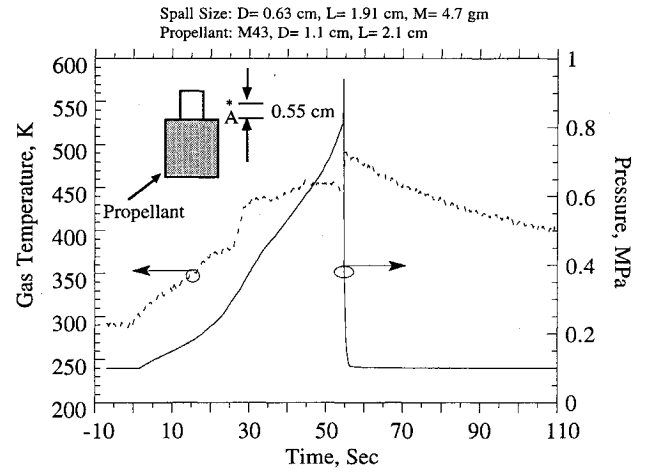

Fig. 6 Recorded temperature and pressure-time traces for M43 propellant in an HFCI test (initial spall temperature = 1023 K).

burning reached that position. The M43 sample was almost completely consumed by pyrolysis, ignition, and combustion. Only a trace of residue remained. The pressure in the chamber remained at 1 atm throughout this test and is therefore considered as one of the partially confined test cases.

Figure 4 illustrates a typical set of recorded temperature- and pressure-time traces in a test using XM39 propellant in a highly confined enclosure. Note that only a negligibly small amount of gas departed from the test rig. The initial temperature of the spall fragment, with a 1.91 cm (0.75 in.) length, was 1123 K. Thermocouple A, used to record the gas-phase temperature, was placed 0.55 cm above the top surface level of the propellant. Inspection of Fig. 4 reveals that the gas accumulation of pyrolysis products caused pressure to build up in the chamber. In the early period, the gas temperature and pressure increased gradually due to pyrolysis and decomposition of the propellant, and no luminous flame was observed. At t = 43 s, gas-phase reactions were violent, and a luminous flame was observed within the entire chamber. As a result, the gas temperature and pressure increased rapidly, which is an indication of gas-phase ignition. This rapid ignition caused an abrupt pressure rise from 0.515 to 0.86 MPa. The diaphragm rupture at 0.86 MPa resulted in rapid depressurization of the chamber, flame disappearance, and quenching of the propellant combustion.

Figure 5 also shows the recorded gas-phase temperature- and pressure-time traces caused by pyrolysis of the XM39 propellant in a highly confined enclosure. The propellant was subjected to a spall fragment of the same size as in the previous case, but with a lower initial temperature of 1023 K. Upon contact with the spall fragment, the chamber quickly filled with a brownish gas. The gas temperature and pressure gradually increased, but the rate of pressurization was much slower than that of the previous case. Because no significant exothermic reaction occurred in the gas phase, the gas temperature remained steady for about 40 s. At this time, the propellant was completely consumed by pyrolysis. As a result, the gas temperature began to decrease due to heat loss to the chamber wall, and the pressure, therefore, also decreased slowly. No sign of ignition (usually accompanied with a visible luminous flame and an audible diaphragm rupture) was observed in this test. The mass loss of the XM39 propellant due to pyrolysis was much larger in the highly confined enclosure than in the partially confined enclosure.

In a highly confined enclosure, Fig. 6 displays the recorded temperature- and pressure-time traces for the M43 propellant that was first pyrolyzed immediately upon contact with the hot spall cylinder and finally ignited at 55 s. The propellant was subjected to heating by a spall fragment of the same size and initial spall temperature of 1023 K, as in the previous case using XM39 propellant (see Fig. 5). The thermocouple used to record the gas-phase temperature was placed 0.55 cm above the top sample surface level. After the spall fragment landed on the top surface of the propellant, the propellant slowly produced pyrolysis gases that filled the chamber during the first 50 s. At t = 55 s, the species in the gas phase reacted violently and a luminous flame was observed within the entire

chamber. At the same time, the gas temperature and pressure went up rapidly. The sound from the rapid gas-phase reaction and diaphragm rupture was heard immediately after the luminosity was observed within the test chamber. The pressure rose sharply from 0.79 to 0.96 MPa, followed by a rapid chamber depressurization due to rupture of the diaphragm. Thus, the propellant combustion was quenched. Approximately 0.18 gm of unburned propellant was recovered.

Figure 7 shows a set of recorded pressure-time traces for the M43 propellant in a highly confined enclosure for various initial spall temperatures ranging from 773 to 1123 K. The mass of the stainless steel spall fragment (4.7 gm) was held constant during this series of tests. As clearly depicted in this figure, the ignition delay time increases with the decrease of the initial spall temperature. Ignition was reached at 112 s for the test with the spall initial temperature at 793 K. The go/no-go ignition boundary for M43 propellant heated under this highly confined condition lies between 773–793 K. It is interesting to note that this ignition temperature range is about 650 K lower than the ignition temperature of the same propellant heated under nearly constant pressure conditions of 1 atm.

B. Go/No-Go Ignition Boundaries for Nitramine-Based Propellants

Figure 8 shows the go/no-go ignition boundaries of XM39 and M43 propellants in both partially and highly confined environments. The change in the mass of the cylindrical fragment was achieved by altering its height; the diameter was held constant at 0.63 cm. As expected, the minimum fragment temperature for igniting XM39 and M43 propellants was found to decrease with increasing fragment mass. As the mass of the spall fragment was increased, its heat content also increased. Smaller fragments require a higher initial temperature to ignite a propellant.

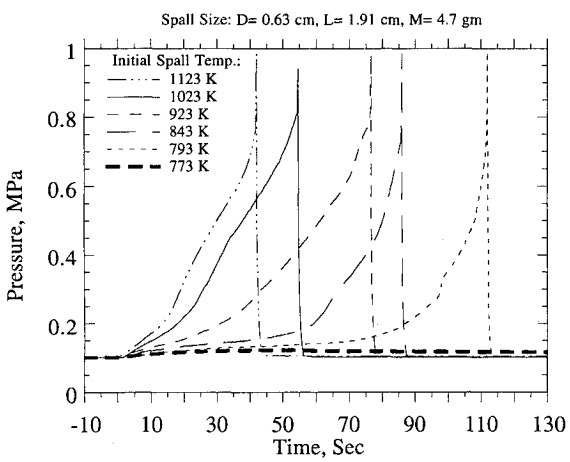

Fig. 7 Recorded pressure-time traces for M43 propellant in a highly confined enclosure for various initial spall temperatures.

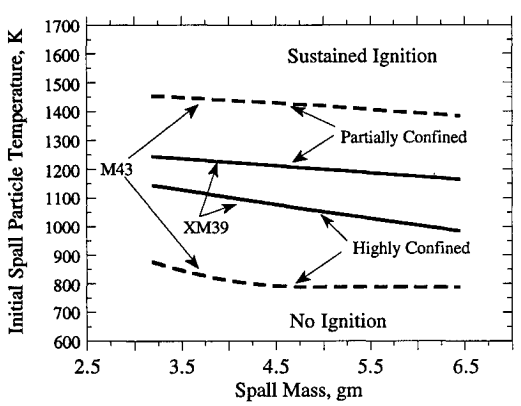

Fig. 8 Experimental go/no-go ignition boundaries for XM39 and M43 propellants in different confined enclosures.

The XM39 propellant was found to be more susceptible to conductive ignition by the spall fragment than the M43 propellant in the partially confined enclosure. For example, with a 3.2-gm fragment, the ignition temperature of M43 measured was about 1473 K, the maximum temperature of spall heated by tube furnace, but the ignition temperature of the XM39 propellant was about 1273 K, 200 K lower than that of the M43 propellant.

Under highly confined conditions, which allow for chamber pressurization, the M43 ignition threshold becomes lower than that of XM39. For example, with a 6.4-gm fragment, the measured ignition temperature of M43 was about 823 K, but the ignition temperature of the XM39 propellant was about 1023 K, 200 K higher than that of the M43 propellant. This result can be used to explain the unexpected ignition behavior of the M43 propellant observed in shaped-charge jet impact tests of cartridges where the M43 propellant grains may lead to a pressure rise caused by an accumulation of pyrolysis products within the cartridge and subsequent gas-phase ignition among pyrolysis products.[1]

By comparing of the experimental go/no-go ignition boundaries between partially and highly confined enclosures, the extent of the chamber confinement was found to have a significant effect on the go/no-go ignition boundaries, especially in the case of the M43 propellant. In a partially confined environment, the pressure of the gas-phase region remains at 1 atm, and ignition most probably occurs in the foam layer. An extremely high initial spall temperature is needed to ignite the propellant. In a highly confined environment, the chamber pressure reaches several atmospheres prior to rapid gas-phase ignition. Even at a much lower initial spall temperature, the propellant can still be ignited.

V. Theoretical Results and Discussion

Governing equations for heat conduction within the spall particle and inert heating of the propellant were recast into ordinary differential equations by the integral method.[11] The overall PCHFCI model consists of a total of 34 ordinary differential equations solved simultaneously by Gear's method.[12]

A. Temperature and Pressure Variations for XM39 Propellant

Figure 9 depicts the calculated time variations of temperature and pressure for the XM39 propellant in a partially confined enclosure ($A_{exit} = 3.17 \times 10^{-5}$ m^2). The spall size of $L_s = 1.27$ cm and $R_s = 0.317$ cm with an initial spall temperature of $T_{si} = 1203$ K was employed in the numerical simulation. Initially, the solid propellant was subjected to an inert heating period of about 1 s duration. Once the inert heating period was complete, both the calculated gas-bubble and liquid-phase temperatures increased rapidly. The initial temperatures of the liquid T_{lf} and gas T_{gf} in the foam layer were assumed to be 460 K. Peak values of these temperatures occur 3 s after the spall impact, and beyond these peaks, the foam-layer temperatures gradually decrease due to heat losses to the propellant and surroundings. The temperature along the bottom surface of the spall T_{SB} decreases due to heat transfer to the foam layer by conduction and to the gas-phase region by both convection and radiation. The thermal response by the gas-phase region T_g is delayed slightly, but rapidly reaches a value of about 530 K and then reduces gradually. Because of the relatively small size of the spall fragment and its low heat-transfer coefficients, its contribution to heating the gas-phase region is small; most of the spall's energy is conducted into the foam layer. Since calculations showed a gradual decrease in all temperatures beyond a time span of about 3 s, no ignition was predicted. In the partially confined enclosure ($A_{exit} = 3.17 \times 10^{-5}$ m^2), the accumulation of pyrolysis products does not cause a pressure rise within the enclosure. The pressure remained steady at 1 atm.

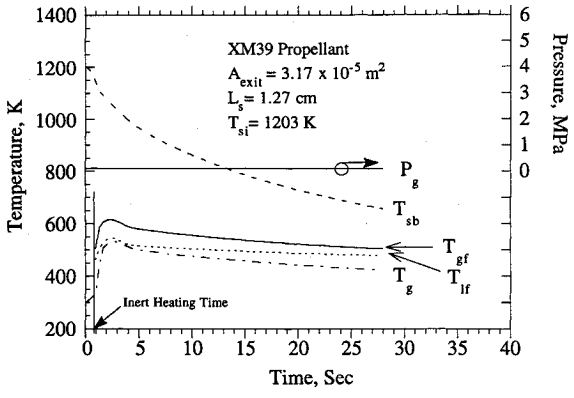

Fig. 9 Calculated time variations of temperatures and pressure for XM39 propellant (initial spall temperature = 1203 K).

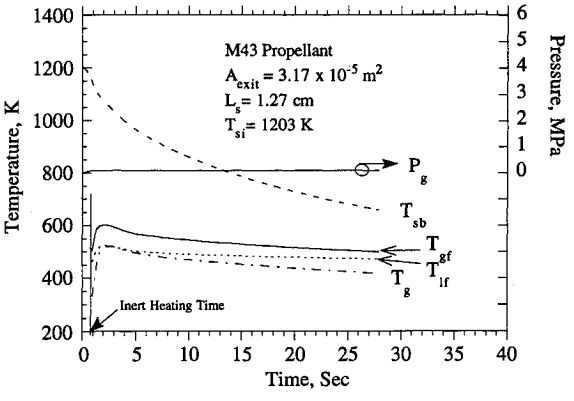

Fig. 10 Calculated time variations of temperatures and pressure for M43 propellant (initial spall temperature = 1203 K).

B. Species, Temperature, and Pressure Variations for M43 Propellant

Figure 10 illustrates the calculated time variations of temperatures and pressure when the M43 propellant is subjected to the heating of a spall fragment of the same size and initial temperature as in the previous case. The decomposition of the EP in M43 propellant is more endothermic than that of ATEC in XM39 propellant. Therefore, the temperatures of the T_{lf} and T_{gf} in the foam layer in the M43 propellant were slightly lower compared to those in the XM39 propellant. The T_{SB} decreases due to heat transfer to the foam layer by conduction and to the gas-phase region by both convection and radiation. Again, no ignition was predicted.

Figure 11 shows the calculated species mass fractions in the gas-phase region for the same simulation case for M43 propellant. Due to pyrolysis and decomposition of the propellant, the mass fractions of CH_2O and NO_2 increase near the end of the inert heating period. Examination of the calculated results reveals no rapid reaction between CH_2O and NO_2 species, and the extent of RDX decomposition is quite limited.

C. Effect of Chamber Exhaust Port Size on Ignition

To study the effect of the chamber exhaust port size on ignition of the M43 propellant within a partially confined enclosure, two different sizes of chamber exhaust ports (3.17 $\times$ 10^{-5} and 3.17 $\times$ 10^{-9} m^2) were considered for simulation, using the same size of spall particles (L_s = 1.27 cm and R_s = 0.317 cm) and a spall initial temperature of 1203 K.

For the larger opening case (see Figs. 10 and 11), accumulation of pyrolysis products is limited, causing essentially no buildup of temperature and pressure within the enclosure. The calculated time variations of temperature, pressure, and species composition in the gas-phase region indicated that no ignition occurred. For the smaller size opening case (shown in Figs. 12 and 13), the pressure inside the enclosure increased above the ambient pressure. Self-sustained ignition occurred at about 7 s when the rate of heat generated by the exothermic reactions exceeded the rate of heat loss. It is of interest to observe that the predicted mass fraction of NO_2 is higher than that of CH_2O in the gas phase for the M43 propellant and is opposite to that for the XM39 propellant.

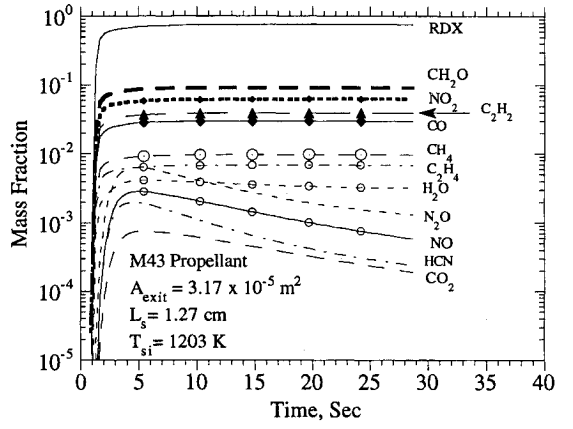

Fig. 11 Calculated time variations of species composition in gas-phase region for M43 propellant.

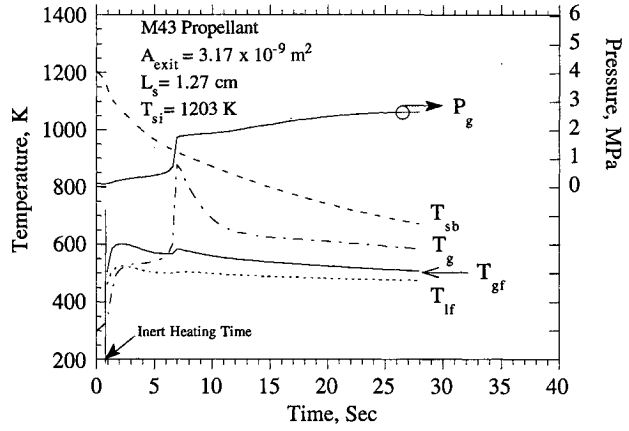

Fig. 12 Calculated time variations of temperatures and pressure for M43 propellant in a highly confined enclosure.

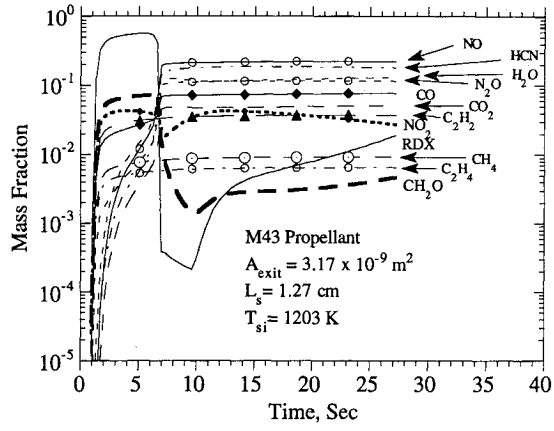

Fig. 13 Calculated time variations of species composition in gas-phase region for M43 propellant in a highly confined enclosure.

D. Go/No-Go Ignition Boundaries of Nitramine-Based Propellants

Figure 14 shows the calculated go/no-go ignition boundary in terms of initial spall temperature vs chamber exhaust port

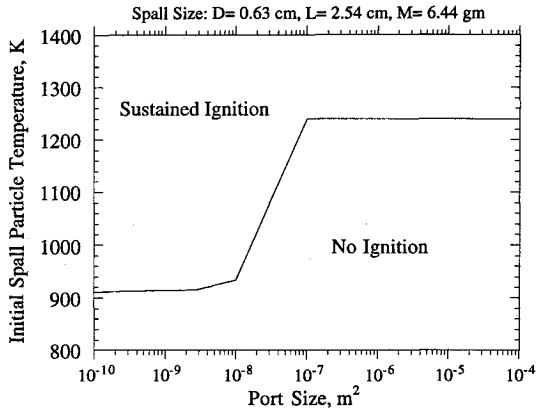

Fig. 14 Calculated go/no-go ignition boundary in terms of initial spall temperature versus exhaust port size for XM39 propellant.

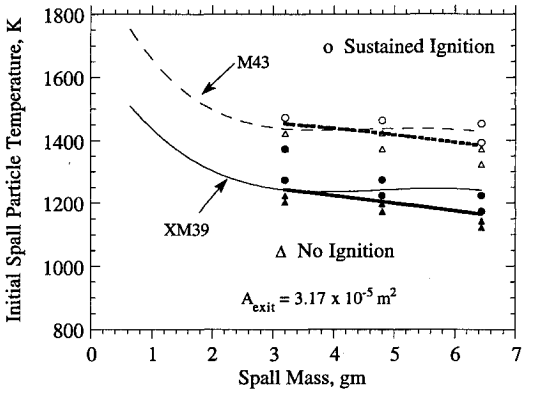

Fig. 15 Comparison of experimental data with calculated go/no-go ignition boundaries for XM39 and M43 propellants in a partially confined enclosure.

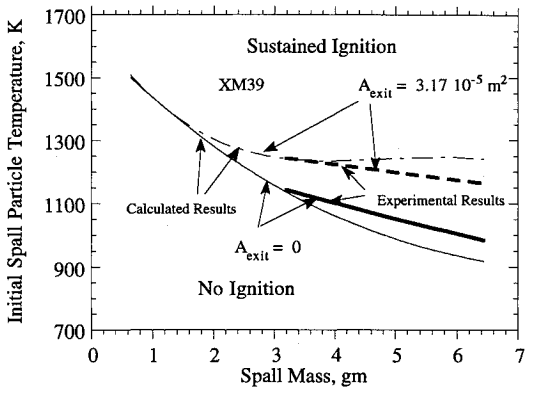

Fig. 16 Comparison of experimental data with calculated go/no-go ignition boundaries for XM39 propellant in different confined enclosures.

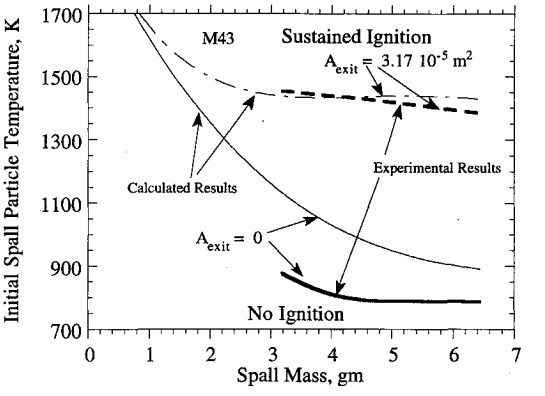

Fig. 17 Comparison of experimental data with calculated go/no-go ignition boundaries for M43 propellant in different confined enclosures.

size for the XM39 propellant. The size of the spall fragment was held constant at 6.4 gm mass with a geometry of 2.54 cm length and 0.63 cm diameter. For an exit area larger than 10^{-7} m^2, pressure cannot be built up by accumulation of pyrolysis product gases. Therefore, the minimum ignition temperature is approximately 1240 K. For an opening area smaller than about 10^{-7} m^2, the pressure inside the enclosure increases to levels above the ambient pressure. The exothermic reaction between CH_2O and NO_2 species is enhanced under gas accumulation conditions, which reduces the ignition threshold to T_{si} = 920 K as the chamber approaches a highly confined environment.

Figure 15 shows the calculated and experimentally determined go/no-go ignition boundaries for a partially confined enclosure ($A_{exit} = 3.17 \times 10^{-5}$ m^2). The calculated ones, for partially confined environments, were found to be in very good agreement with the measured data. The XM39 propellant was found to be more susceptible to ignition than the M43 propellant in a partially confined environment. The reason the M43 propellant is more resistive to conductive ignition is that its binder decomposition is more endothermic and the foam-layer ignition occurs only at an extremely high initial spall-fragment temperature.

Figure 16 presents a comparison of experimental data with calculated go/no-go ignition boundaries for XM39 propellant in different confined enclosures. Both theoretical calculations and experimental data show that the go/no-go ignition boundary of the highly confined case is lower than the partially confined case. The calculated go/no-go ignition boundaries of XM39 propellant for the range of spall fragment sizes tested are consistent with the measured values. Smaller spall fragments were not used in experimental measurement since they must be heated to temperatures beyond the maximum temperature of the furnace. Figure 17 compares experimental data with calculated go/no-go ignition boundaries for the M43 propellant in different confined enclosures. For the M43 propellant, the extent of the chamber confinement was found to have an even stronger effect on the go/no-go ignition boundaries than XM39 propellant. For a larger size spall within a highly confined enclosure, the M43 propellant was found to be more vulnerable to HFCI than the XM39 propellant. Although the match of the highly confined case is not extremely close, calculated results show the same trend and are also useful in explaining the unexpected ignition behavior observed in shaped-charge jet impact tests of cartridges loaded with M43 propellant grains.[1] In these tests, penetration of spall fragments through the cartridge case could therefore lead to a pressure rise caused by an accumulation of reactive pyrolysis products such as NO_2 and CH_2O within the cartridge. Exothermic reactions between these gaseous species could cause subsequent gas-phase ignition and further chamber pressurization.

VI. Summary and Conclusions

A comprehensive theoretical and experimental investigation has been carried out to characterize the ignition behavior of XM39 and M43 propellants in partially and highly confined enclosures. In the experimental portion, a test rig was designed and constructed for dropping a heated steel cylinder at a known initial temperature onto a propellant sample. In the theoretical portion, an existing HFCI model was extended by incorporating a reduced chemical kinetic mechanism and by accounting for the effect of gas accumulation in the partially confined environment. The effects of initial temperature of spall particle, size of spall particle, and size of chamber exhaust port were examined.

The go/no-go ignition boundaries were predicted for both XM39 and M43 propellants under various degrees of confinement. Good agreement was obtained between the calculated and experimentally determined the go/no-go ignition boundaries for these propellants in a partially confined enclosure in which the pressure was maintained at 1 atm prior to ignition. Both calculated results and experiment data show the shift of the go/no-go ignition boundary from the highly confined case to that of a partially (weakly) confined condition. The XM39 propellant was found to be more susceptible to ignition by the spall fragment than the M43 propellant at low pressures because binder decomposition of the M43 propellant is more endothermic than that of the XM39 propellant. At highly confined conditions that allow for chamber pressurization, the M43 ignition threshold became lower than that of XM39 propellant. It is believed that the reduction of ignition threshold is caused mainly by the exothermic reaction between CH_2O and NO_2 species; their concentrations and collision rates are increased under chamber pressurization conditions. This effect is more pronounced for the M43 propellant, which generated a higher concentration of NO_2 from its energetic plasticizer.

VII. Future Research

The preceding discussion of results was focused on an overall assessment of 1) the thermochemical processes controlling the ignition susceptibility of XM39 and M43 propellants and 2) the unexpected ignition behavior of M43 propellants within confined enclosures. Because of the lack of detailed knowledge of binder decomposition kinetics, a thorough discussion about the established temperatures in the gas-phase region and foam layer, the effects of basic input data (such as liquid-to-gas conversion rates, heat transfer coefficients, etc.), has been omitted. Future research efforts should be focused on experimentally determining the products and rates of binder decomposition, bulk temperature variations in gas-phase region, the effect of free volume size, role of other reactions on the ignition susceptibility, and the possible condensation of NO_2 on chamber walls.

Acknowledgments

This work was performed under Contract DAAL03-92-G-0020 and supported by D. M. Mann of the U.S. Army Research Office, Research Triangle Park, North Carolina. The authors gratefully acknowledge the support provided by J. M. Heimerl of the Army Research Laboratory, Aberdeen Proving Ground, Maryland. The authors also acknowledge the assistance of K. C. Hsieh of NASA Lewis Research Center during the initial phase of the code modification.

References

[1]Raley, B. F., Devynck, D., and Heimerl, J. M., "The Response of the M43 LOVA Propellant to Shaped Charge Jet-Generated Spall," *Proceedings of the 27th JANNAF Propulsion Hazards Subcommittee Meeting* (Albuquerque, NM), CPIA Publ. 526, 1991, pp. 543–551.

[2]Kuo, K. K., Hsieh, W. H., Hsieh, K. C., and Miller, M. S., "Modeling of Hot Fragment Conductive Ignition of Solid Propellants with Applications to Melting and Evaporation of Solid," *Journal of Heat Transfer*, Vol. 110, No. 3, 1988, pp. 670–679.

[3]Hsieh, K. C., Hsieh, W. H., Kuo, K. K., and Miller, M. S., "Modeling of Hot Fragment Conductive Ignition Processes of LOVA Propellants," *Proceedings of the 24th JANNAF Combustion Meeting*, Naval Postgraduate School, Monterey, CA, 1987, pp. 309–324.

[4]Hsieh, K. C., Hsieh, W. H., Kuo, K. K., and Miller, M. S., "Validation of a Theoretical Model for Hot Fragment Conductive Ignition Processes of LOVA Propellants," *Proceedings of the 10th International Symposium on Ballistics* (San Diego, CA), Vol. 1, Sec. 2, 1987, pp. 1–11.

[5]Huang, T. H., Thynell, S. T., and Kuo, K. K., "Modeling of Partially Confined Hot Fragment Conductive Ignition," *25th Symposium (International) on Combustion*, The Combustion Inst., Pittsburgh, PA, 1994.

[6]Brill, T. B., and Brush, P. J., "Condensed Phase Chemistry of Explosives and Propellants at High Temperature: HMX, RDX, and BAMO," *Philosophical Transactions of the Royal Society of London, A*, Vol. 339, 1992, pp. 377–385.

[7]Melius, C. F., "Theoretical Studies of the Chemical Reactions Involved in the Ignition of Nitramines," *Proceedings of the 24th JANNAF Combustion Meeting*, Vol. 1, CPIA Publ. 476, 1987, pp. 359–366.

[8]Miller, M. S., Kotler, A. J., Cohen, A., Truong, K., Puckett, D. L., and Holmes, H. E., "Effective Ignition Kinetics for Lova Propellant," *Proceedings of the 23rd JANNAF Combustion Meeting*, Vol. II, CPIA Publ. 457, 1986, pp. 55–62.

[9]BenReuven, M., Caveny, L. H., Vichnevetsky, R. J., and Summerfield, M., "Flame Zone and Sub-Surface Reaction Model for Deflagrating RDX," *16th Symposium (International) on Combustion*, The Combustion Inst., Pittsburgh, PA, 1976, pp. 1223–1233.

[10]Allen, T., and Ditsworth, R. L., *Fluid Mechanics*, McGraw–Hill, New York, 1972.

[11]Goodman, T. R., "Application of Integral Methods to Transient Nonlinear Heat Transfer," *Advances in Heat Transfer*, edited by T. F. Irvine and J. P. Hartnett, Jr., Vol. 1, Academic, New York, 1964, pp. 52–120.

[12]Hindmarsh, A. C., "Gear: Ordinary Differential Equations System Solver," Lawrence Livermore Lab. Rept. UCID-30001, Rev. 3, 1974.